

# A Geometrical Solution to Einstein’s Equation and its Cosmological Implications

John H. Marr<sup>1</sup>★

<sup>1</sup>*Unit of Computational Science, Bok gebouw, Oort weg 19, 2333, Leiden, NL*

Accepted XXX. Received YYY; in original form ZZZ

## ABSTRACT

A geometrical analysis of the equations of curvature on the manifold in general relativity (GR) suggests that the FLRW metric may admit a subtle modification, with an additional intrinsic curvature term from the expansion of space that is independent of the curvature from mass-energy. The emergence of four new non-zero Christoffel symbols supports the presence of an additional curvilinear motion, and these symbols are distinct from the curvature of space by the presence of mass. Correlation between this modified GR model and the  $\Lambda$ CDM model was assessed using extensive type Ia supernovae (SNe Ia) data, with redshift corrected to the CMB. The modified GR model assumed a value for baryonic mass density of  $\Omega_M = 0.04$ , but required no additional parameters or corrections. The modified GR and  $\Lambda$ CDM models differed by  $^{+0.11}_{-0.15} \mu_B$  mag. over  $z_{cmb} = 0.01 - 1.3$ , with overall weighted RMS errors of 0.136 and 0.151  $\mu_B$  mag. respectively. The models were also fitted to recent baryonic acoustic oscillation (BAO) measures, with weighted RMS errors of  $\pm 0.034$  and  $\pm 0.085$  Mpc and  $H_0 = 67.6 \pm 0.25$  and  $70.0 \pm 0.25$  for the modified GR and  $\Lambda$ CDM models respectively. The modified FLRW metric can describe both the SNe Ia and the BAO observations without requiring dark matter or  $w$ -corrected dark energy, suggesting that GR in its standard form may accept a factor for the curvature of space due to its expansion and may therefore be incomplete.

**Key words:** cosmology: theory – cosmology: observations – distance scale – dark energy – dark matter

## 1 INTRODUCTION

The behaviour of photons in a local gravitational field is well described by General Relativity (GR), and observational data have confirmed without exception that solutions to the general field equations are exact when applied to static or rotating localized gravitational masses. To the early successes of precession of the perihelion of Mercury and gravitational bending of star light during a solar eclipse have been added many other confirmatory observations. These include gravitational redshift (Cottam et al. 2002), the production of Einstein rings by DM halos (Wong et al. 2015), X-ray emission data in the neighbourhood of black holes (Müller & Camenzind 2004; Bromley et al. 2009; Reynolds et al. 2014), and the Sunyaev-Zeldovich effect (Crowell 2012; Planck Collaboration et al. 2016b). As look-back time extends and temperature and energy densities increase towards the CMB radiation and the early universe at  $z \approx 1089$  (Planck Collab-

oration et al. 2016a), gravitational effects on the curvature of the Universe will also clearly have increasing significance.

Curvature occurs in GR by the distortion of space by gravitational energy, but the equations of Friedmann, Lemaître, Robertson, Walker (FLRW) only allow the expansion curvature of SR to be reintroduced by the hyperbolic curvature of space. This contrasts with observations that show space to be essentially flat, but this loss of an innate curvature of expansion may be mimicked in GR by introducing extra mass and a variable acceleration component, as dark matter (DM) and dark energy respectively.

This paper presents a geometrical analysis of the space-time manifold of GR. In addition to the known curvature produced by the enclosed mass-energy density, geometrical analysis suggests that space is fundamentally curved by its own expansion. In the standard model, this curvature is only required for the dust model and is generated by letting space adopt a hyperbolic curvature, but by here adopting an additional curvature term to accommodate the motion of photons across this expansion curvature, the Einstein equations retain the standard components of GR, yet reduce to the

★ E-mail: john.marr@2from.com

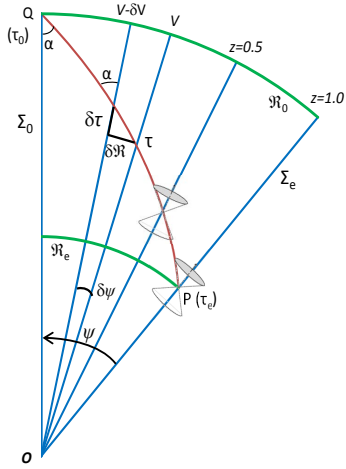


**Figure 1.** Geodesic for photon traversing from frame  $\Sigma_e$  moving at velocity  $V$  relative to  $\Sigma_0$ , and a small element of the geodesic  $\delta S$  for reference frames  $V$  and  $V - \delta V$  rotated through  $\delta\psi$ . The photon path (red line) is then a logarithmic spiral  $1 + z = \exp\psi$  ( $c = 1 \equiv 45^\circ$ ) across diverging galaxies on the complex plane. Redshifts referenced to  $\Sigma_0$ .

equations of SR as  $\Omega_m \rightarrow 0$  without requiring a change in  $\Omega_k$ , the spatial curvature term.

The first postulate of special relativity dictates that the velocity of light is constant for all observers in their local reference frame. Geometrically, this may be represented by the locus of a logarithmic spiral to generate a curve of constant angle to the local time axes (Fig. 1). This geodesic may be illustrated as a curve crossing diverging imaginary time axes, and is independent of the spatial curvature, which is allowed to be flat, spherical or hyperbolic (Marr 2016).

The model is tested by comparing its predictions with the derived apparent magnitude data of supernovae type 1a (Sne 1a) for a large recent data set, and a wide range of recently published angular diameter distances out to  $z = 2.36$ . On both measures, it is comparable to the best  $w$ -CDM model.

## 2 THE FLRW METRIC

A model geometry of the evolving Universe may be constructed as a simply connected smooth Riemannian manifold  $R_m$  with metric  $g_{\mu\nu}$ . It is taken as axiomatic that the Universe is homogeneous and isotropic in space, but not in time. Of the eight Thurston 3-manifold Riemannian geometries, only three fulfil the criteria of homogeneity and isotropy for the observable Universe: the 3-sphere  $S^3$ , the 3-D Euclidean space  $E^3$ , and the 3-D hyperbolic space  $H^3$ . Finite volume manifolds with  $E^3$  geometry are all compact, and have the structure of a Seifert fibre space, remaining invariant under Ricci flow.  $S^3$  manifolds are exactly closed 3-manifolds with finite fundamental group, and under Ricci flow such manifolds collapse to a point in finite time. In contrast, manifolds with  $H^3$  hyperbolic geometry are open and expand under Ricci flow (Milnor 2003). Using a Lie group acting on the metric to compute the Ricci tensor  $R_{\mu\nu}$ , these manifolds are deformed by Ricci flow as a function of time  $t$  and we may

then define the geometric evolution equation,  $\partial_t d_{ij} = -2R_{ij}$ , with normalized Ricci flow given by (Perelman 2008):

$$\partial_t g_{ij} = -2R_{ij} + \frac{2}{3}Rg_{ij}. \quad (1)$$

This is equivalent to a Universe that can be foliated into spacelike slices, and spacetime itself may therefore be represented by  $\Gamma\text{-}\mathbb{R}^3$  where  $\Gamma$  represents the time direction, with the general form  $ds^2 = g_{\mu\nu} dx^\mu dx^\nu$  in the standard notation.  $\mathbb{R}^3$  must be a maximally symmetric space to conform to a homogeneous and isotropic three-manifold, with metric  $d\sigma^2 = \gamma_{ij} dx^i dx^j$ . By scaling  $t$  such that  $g_{00} = -1$  with  $c = 1$ , we may write the metric as:

$$ds^2 = -dt^2 + a(t)^2 \gamma_{ij}(x) dx^i dx^j, \quad (2)$$

where  $\gamma_{ij}$ ,  $x^i$ ,  $x^j$  are the co-moving co-ordinates.

In cosmology, homogeneity and isotropy imply that  $\mathbb{R}^3$  has the maximum number of Killing vectors, and with the additional constraint of the metric being torsion-free (the Levi-Civita connection),  $\gamma_{ij}$  is the maximally symmetric metric of  $\mathbb{R}^3$ . This yields the general solution to Einstein's equation (Misner et al. 1970; Peebles 1993; Carroll 2003), which may be stated in polar coordinates (Eq. 3):

$$ds^2 = -dt^2 + a(t)^2 \left[ dr^2 + S_k^2(r) d\Omega^2 \right], \quad (3)$$

$$\text{where } S_k^2(r) \equiv \begin{cases} \mathfrak{R}_0^2 \sin^2(r/\mathfrak{R}_0) & \text{for } \mathfrak{R}_0 > 0 \\ r^2 & \text{for } \mathfrak{R}_0 = \infty \\ \mathfrak{R}_0^2 \sinh^2(r/\mathfrak{R}_0) & \text{for } \mathfrak{R}_0 < 0, \end{cases} \quad (4)$$

$$\text{or } S_k(r) \equiv \frac{1}{\sqrt{K}} \sin(r\sqrt{K}), \quad (5)$$

and  $K = \text{sgn}(\mathfrak{R}_0)/\mathfrak{R}_0^2$  is the curvature.

With  $\chi$  as a third angular coordinate,  $r = \mathfrak{R}_0\chi$  is the radial distance along the surface of the manifold,  $\mathfrak{R}_0$  is the comoving 4-space radius of  $\mathbb{R}^3$  at the present epoch, and  $d\Omega^2 = d\theta^2 + \sin^2\theta d\phi^2$  is the angular separation. The signature  $\text{diag}(-, +, +, +)$  defines this as a Pseudo-Riemannian manifold with metric  $g_{\mu\nu}$  and spatial metric  $g_{ij}$ , and  $a(t)$  is the scale factor at proper time  $t$ . The actual form of  $a(t)$  is determined by the curvature of the manifold and the energy tensor of Einstein's field equations, with curvature  $K$  (or radius  $\mathfrak{R}$ ), and scale factor  $a(t)$  to be determined.

Intrinsic curvature is a mathematical construct relating the deviation of parallel lines towards or away from each other, and does not require higher dimensions. However, to understand physical reality we may invoke geometrical representations, with intrinsic curvature equivalent to embedding in higher dimensions, and this geometric dimensionality is distinct from other attempts to introduce extra physical dimensions into GR by quantum gravity or string theory (Figueras et al. 2016).

It should be emphasized that—just as the surface of a sphere is a curved 2-D manifold embedded in Euclidean 3-space—so this manifold is a curved 3-D volume embedded in Euclidean 4-space. Measurements on the surface of a 2-D sphere involve a distance and an angle, with the third dimension the implicit radius of the sphere. For the 3-D volume,  $\chi$  is a third extra angular measure, with the implicit radius  $\mathfrak{R}$  the fourth dimension (Komissarov 2009). For an

expanding 2-D manifold in 3-D space, time is a fourth dimension, and—by extension—for the expanding 3-D volume the time axis represents a fifth dimension. The curvature or shape of the homogeneous hyper-surfaces are defined by the spatial 3-metric  $\gamma_{ij} dx^i dx^j$  of Eq. 2, but the whole dynamics of the Universe are embodied only in the expansion factor,  $a(t)$  (Misner et al. 1970).

With  $r$  as the radial coordinate, radial distances are Euclidean but angular distances are not. If we are only interested in photon redshift distances,  $d\Omega = 0$  and Eq. 3 is the more useful form of the metric. Setting  $ds^2 = 0$  and  $g_{\theta\theta} = g_{\phi\phi} = 0$ ,  $dr$  now represents a radial photon distance from the era of emission  $t_e$  to the present epoch at  $t_0$ , with:

$$R_y = \int dr = \int_{t_0}^t \frac{dt}{a(t)}. \quad (6)$$

$R_y$  is a function of  $a(t)$  only, and may be independent of the curvature of the spatial manifold. Symmetry ensures that proper time for standard clocks at rest relative to the spatial grid is the same rate as the cosmological time ( $t$ ), making the interval  $dt$  Lorentzian. Any coordinate system in which the line element has this form is said to be synchronous because the coordinate time  $t$  measures proper time along the lines of constant  $x^i$  (Misner et al. 1970).

The substitution  $\chi = \sin(r/\mathfrak{R})$ ,  $\chi = r/\mathfrak{R}$ , or  $\chi = \sinh(r/\mathfrak{R})$  into  $S_k(r)$  in Eq. 3 makes  $\chi$  a radial coordinate with  $\mathfrak{R}$  absorbed into  $a(t)$ , and angular distances are Euclidean but radial distances are not (Eq. 7):

$$ds^2 = -dt^2 + \mathfrak{R}(t)^2 \left[ \frac{d\chi^2}{1 - k\chi^2} + \chi^2 d\Omega^2 \right]. \quad (7)$$

This form is useful for measuring angular distances on a shell of fixed radius ( $g_{\chi\chi} = (1 - k\chi^2)^{-1}$ ,  $d\chi = 0$ ), such as the proper diameters of clusters or spatial volume for galaxy counts.

### 3 THE EXPANDING UNIVERSE AS GEOMETRY

Milne described a dust universe expanding with constant relative velocity assigned to each galaxy, and with a mass-energy density sufficiently low that any deceleration could be neglected (Milne 1935). Such a universe does not have to be spatially flat, but it does have the property that  $\dot{a}(t) = \text{constant}$ , and hence  $a(t) = a_0(t/t_0)$ , where  $a_0$  is the scale factor at the current epoch  $t_0$ , defined to be  $a_0 = 1$ . Taking Eq. 3 to be the FLRW metric for the photon path, we may state that  $d\theta = d\phi = 0$ , and hence  $d\Omega = 0$  and consider only the radial coordinate  $dr$ . This modified Milne model (M3) is therefore independent of the space curvature: this may be an expanding 3-sphere, a flat 3-sheet, or a 3-saddle. What M3 does demand is that the time-like foliation of these 3-spaces is linear; the space itself may be infinite or closed, but will maintain its initial curvature signature whether expanding forever or contracting.

Einstein's first postulate in a system of non-accelerating inertial frames may be summarized as: the velocity of light is constant for any observer, independent of the velocity of the source. Interpreting the time coordinate as the imaginary axis has become depreciated, but to do so forces the proper

time axis to be a radius of length  $\tau = ict$  and allows a graphical interpretation of the interval  $S$  to be unvarying under rotation, providing a geometric visualization to this postulate (Marr 2016). In Figure 1, the infinitesimal geodesic is extended to illustrate the path of photons between galaxies in the uniformly expanding homogeneous, isotropic universe of M3.

This geometrical figure is generated by assuming that: (1) observed redshifts represent a true relative motion (whatever the underlying cause); (2) galaxies are moving apart with a velocity that is constant over the time period of the observations, generating a set of diverging inertial reference frames in space; (3) photons traverse these reference frames at constant velocity  $c$  to all local observers, in their local Minkowski space under a Lorentzian transformation.

Any individual volume of space such as a specific galaxy may be considered stationary within its own reference frame. Let us define this reference frame as  $\Sigma_0$  for our own local galactic space (Fig. 1). This neglects small-scale local movements, being a simple representation and first order approximation of an idealized world line for a particle in space, because the components of  $v$  are assumed to relate only to local motions that are generally much less than the recession velocity, and are taken to be zero in most theoretical models of the Universe.

The relative motion of two inertial frames,  $\Sigma_0$  and  $\Sigma_e$ , diverging from a common origin with velocity  $v$  may then be viewed as a hyperbolic rotation  $\psi$  (the rapidity) of the spacetime coordinates on the imaginary plane (Fig. 1), a Lorentz boost with a rotational 4-matrix  $\Lambda_{\nu'}^{\mu}$ :

$$x^{\mu} = \Lambda_{\nu'}^{\mu} x^{\nu'} \quad (8)$$

$$\Lambda_{\nu'}^{\mu} = \begin{pmatrix} \cosh \psi & \sinh \psi & 0 & 0 \\ \sinh \psi & \cosh \psi & 0 & 0 \\ 0 & 0 & 1 & 0 \\ 0 & 0 & 0 & 1 \end{pmatrix}$$

where  $\cosh \psi = (1 - v^2/c^2)^{-1/2} = \gamma$ ,  $\sinh \psi = \beta\gamma$ , and  $\tanh \psi = \beta = v/c$ , in the standard notation, with  $\det \Lambda = +1$ .

Now consider a volume of space receding from us with velocity  $v$  as defined by its redshift, with a proper radial distance  $\mathfrak{R}_e$  at the time of emission. The photon path is now represented geometrically as a logarithmic spiral on the complex plane ( $PQ$  in Fig. 1). It will be noted that  $\psi$  is the hyperbolic angle, so the geometry allows  $\psi > 360^\circ$  because  $v/c = \tanh \psi \rightarrow 1$  as  $v \rightarrow c$  and  $\psi \rightarrow \infty$ , whereas local velocities are represented by real angles with trigonometric functions. The scale is chosen by convention such that  $\alpha = 45^\circ$  with  $c = 1$ , hence the maximum angle in the local frame of reference corresponds to the standard light cone with  $\text{atan}(1) = 45^\circ$ . Although the spatial component of the M3 model may have curvature, M3 has no matter density and Fig. 1 is therefore geometrically flat as a consequence of the linear relationship between the radial and time axes.

For a photon,  $\delta S = 0$  (null geodesic for photon). It then follows that  $\delta \mathfrak{R}^2 = c^2 \delta t^2$ , or  $\delta \mathfrak{R} = \pm c \delta t$ , where the sign represents an incoming or outgoing photon. But  $\delta \mathfrak{R} = ct \delta \psi$ , thus  $\delta t/t = \mp \delta \psi$ . Using  $-\delta \psi$  for the incoming photon and integrating:

$$\int_{t_e}^{t_0} \frac{dt}{t} = \int_{\psi}^0 -d\psi. \quad (9)$$

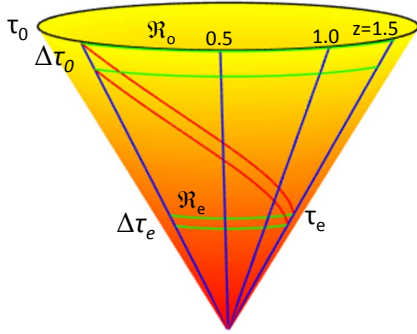


**Figure 2.** The Milne manifold of Fig. 1 as a 3-D cone for two photons crossing expanding space, originating at redshift  $z = 1.5$  and crossing the paths of galaxies at redshift 1.0 and 0.5 at constant ( $45^\circ$ ) angle. The increase in  $\Delta\tau_e$  to  $\Delta\tau_0$  (or equivalently from  $\lambda_e$  to  $\lambda_0$ ) is visualized in this exaggerated plot.

$$\text{i.e. } \ln(t_0/t_e) = \psi \text{ or } t_0/t_e = e^\psi. \quad (10)$$

Although all diverging world lines are equivalent and will “see” photons intercepting and leaving them at velocity  $c$ , the source lines are Doppler red-shifted with a wavelength of emission  $\lambda_e$  in  $\Sigma_e$ , and a wavelength at observation  $\lambda_0$ . Redshift is defined as:

$$z = \frac{\lambda_0 - \lambda_e}{\lambda_e} = \lambda_0/\lambda_e - 1 \quad (11)$$

and setting  $\lambda_e = \Delta t_e$ ;  $\lambda_0 = \Delta t_0$ , it is easy to show that

$$1 + z = \Delta t_0/\Delta t_e = t_0/t_e = e^\psi. \quad (12)$$

But  $e^\psi = \cosh \psi + \sinh \psi$ , hence

$$1 + z = \gamma + \gamma\beta = \gamma(1 + \beta), \quad (13)$$

which is the relativistic Doppler shift in SR, with  $z \rightarrow \infty$  as  $v \rightarrow c$ .

We may perform a topological transform of the Milne model of Fig. 1 into an imaginary 4-cone (Fig. 2) without loss of generality. From Eq. (12),  $\psi = \log(1 + z)$ , and the three galaxies represented in Fig. 2, with redshifts of 0.5, 1.0 and 1.5, have corresponding hyperbolic angles of  $\psi = 23.2^\circ$ ,  $39.7^\circ$ , and  $52.5^\circ$  respectively.

Despite the appearance of curvature, there is no acceleration ( $\dot{a} = \text{constant}$ ;  $\ddot{a} = 0$ ) and this remains a topologically flat figure. The imaginary proper time axes (e.g.  $\tau_0$  and  $\tau_e$ ) are straight lines that diverge linearly. Likewise, the radii of curvature round the vertical axis are proportional to  $a(t)$ , the radial distances on the manifold at constant cosmological (proper) times (e.g.  $\mathfrak{R}_0$  and  $\mathfrak{R}_e$ ) are orthogonal functions of  $a(t)$  only, and the locus of each photon track is a line of constant angle.

#### 4 GR AS GEOMETRY

The presence of mass-energy in the Universe introduces a non-linear component to  $a(t)$  with consequent curvature of the time axis, and an additional curvature to the path of the photon. This cannot be displayed on a flat 2-D diagram, but can be demonstrated using the topological transform

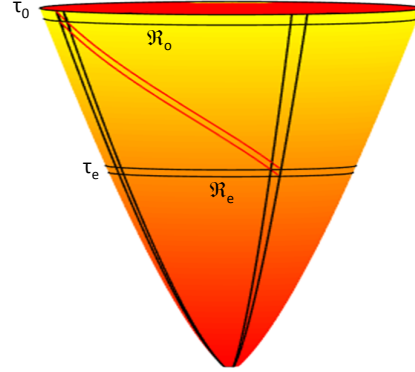


**Figure 3.** The cone manifold of Fig. 2 with curvature of the imaginary time axis by the presence of matter, and two photons crossing expanding space at constant angle.

of Fig. 2. The presence of acceleration introduces curvature to the imaginary  $\tau$  coordinate (Fig. 3), representing accelerations from gravitational or dark mass and dark energy that may be attractive/positive or negative/repulsive respectively.

The manifold of a sphere in 3-space is sufficiently described as a curved two-dimensional surface. Similarly the extra dimensions required to visualize the geometry of expanding curved spacetime do not represent real dimensions, but are a helpful aid to geometrical visualization of the manifold. Because 3-space with curvature require a 4-dimensional space and the curved time coordinate occupies a further dimension, space-time now exists in 5-space, compacted in Fig. 3 to a 2-manifold in 3-space. Integration of the photon path across this surface may be represented by considering a thin wedge or petal of the time-space manifold in GR (Fig. 4), with the imaginary surface curved by mass-energy as well as by expansion.

The new radius of curvature is  $R(\tau) = 1/(d\beta/d\tau)$ , and this is independent of the spacial curvature,  $K$ . In the Milne model, the manifold is flat with  $d\beta/d\tau = 0$ , and  $R = \infty$ , and the cone base angle,  $\beta_0$ , can take any arbitrary value, with  $\beta_0 = \pi/2$  for Fig. 1. Referring to Fig. 4, the lines of longitude are the imaginary time axis, with  $d\tau = i dt$ , whilst the lines of latitude represent the spatial component defined by  $dL = \gamma_{ij}(x) dx^i dx^j$  (Eq. 2);  $\Delta L_0$  is the comoving distance;  $\Delta L = a(t)\Delta L_0$  is the proper distance at time  $t$ ; and the curvature  $1/R^2 = f(\ddot{a})$  is the acceleration. It may be noted that—in contrast to a general *radius v. time* plot with  $t$  as the vertical axis—the time axis is here embedded in the manifold. Unlike Fig. 2, the apex of this cone does not converge onto the vertical axis, but curls round itself as  $\ddot{a} \rightarrow 0$ . The model therefore still requires an inflationary scenario to close the gap and ensure causal connectedness.

#### 5 GEOMETRY WITH CURVATURE

Geometrically, redshift is observed when otherwise parallel photon paths deviate away from each other, as evidenced in the flat Minkowsky Milne model of Fig. 1. The modified GR model is an attempt to present the geometrical curvature of diverging (redshifted) photons as a clear but separate curvature superimposed on both the secondary curvature of

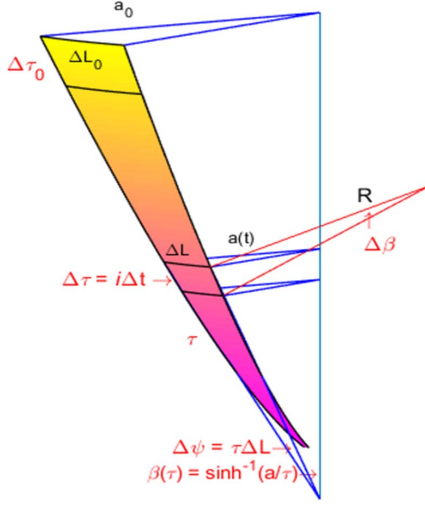


**Figure 4.** Thin slice of curved GR manifold,  $\Delta L$  vs.  $\tau$ . Imaginary values are shown in red.  $\Delta\beta = \Delta\tau/R$  is rate of change of expansion;  $\beta = \sinh^{-1}(a/\tau) = f(H)$ . (The mass-energy radius of curvature,  $R$ , is considerably foreshortened in this exaggerated plot)

spacetime through gravitational mass and any intrinsic primary curvature of space itself.

Standard vectors are restricted in the presence of curvature on the spacetime manifold, but we may use Cartan vectors as operators (Komissarov 2009). Assign to each particle in the Universe the set of observer-dependent coordinates  $x^\mu$ . This represents an invariant line element with proper time  $x^0 = t$ , whose spacetime geometry is encoded in the metric  $ds^2 = g_{\mu\nu} dx^\mu dx^\nu$ , with space coordinates  $x^i = x^i(t)$ . Free particles then move along curved geodesics, with 4-velocity

$$U^\mu = \frac{dx^\mu}{ds}. \quad (14)$$

With  $t$  as a parameter, the spatial derivatives are the velocity components  $U^i = dx^i/dt$ , and we may introduce the differential operator  $d/dt = U^i \partial/\partial x^i$ , which is the directional derivative along the curve (Komissarov 2009). The components  $U^i$  of the operator now form the local coordinate basis,

$$\vec{U} = \frac{d}{dt}; \quad \vec{e}_i = \frac{\partial}{\partial x^i}, \quad (15)$$

and the basis vectors  $\vec{U} = U^i \vec{e}_i$  define the parametrized vector space associated with the point  $x^\mu$ .

Acceleration may be expressed in terms of Eq. 14:

$$\frac{dU^\mu}{ds} = \frac{\partial U^\mu}{\partial x^\alpha} \frac{dx^\alpha}{ds} = U^\alpha \frac{\partial U^\mu}{\partial x^\alpha}. \quad (16)$$

Their motion is then described by the geodesic equation:

$$\frac{dU^\mu}{ds} + \Gamma_{\alpha\beta}^\mu U^\alpha U^\beta = 0, \quad (17)$$

$$\text{i.e. } U^\alpha \left( \frac{\partial U^\mu}{\partial x^\alpha} + \Gamma_{\alpha\beta}^\mu U^\beta \right) \equiv U^\alpha \nabla_\alpha U^\mu = 0, \quad (18)$$

where the Christoffel symbols are defined by:

$$\Gamma_{\alpha\beta}^\mu = \frac{1}{2} g^{\mu\lambda} (\partial_\alpha g_{\beta\lambda} + \partial_\beta g_{\alpha\lambda} - \partial_\lambda g_{\alpha\beta}). \quad (19)$$

## 5.1 Curvature of space from the velocity vector

Parallel transport of a vector is different over different paths. For redshift observations, we are interested in the parallel transport of photons across an expanding space, whose rate of expansion changes with time and distance. The standard FLRW metric is generally written as a symmetrical function (Eq. 2), with  $\mu, \nu = 0 \dots 3$ . However, as demonstrated in Section 2, the  $R$ -axis may have one further curvature representing the divergence of space as a consequence of its expansion. This requires an additional dimension represented by  $z' = \tau \cos i\psi = \tau \cosh \psi$  on the imaginary plane, with divergent angle  $\psi$ , and  $\mu, \nu = 0 \dots 4$ . Unlike local velocities that are represented by real angles with trigonometric functions, because  $\psi$  is a hyperbolic angle this geometry allows  $\psi > 360^\circ$ .

In contrast to SR, this divergence velocity is not a physical separation velocity in a static space, but an observational velocity defined by the redshift of space itself, and this introduces a new component  $\gamma_{\psi\psi} = \tau^2 \sinh^2 \psi$  to the geodesic equation (Eq. 20):

$$ds^2 = -dt^2 + \gamma_{ij}(x) dx^i dx^j + \tau^2 \sinh^2 \psi d\psi^2. \quad (20)$$

The time component to the geodesic is  $-dt^2$ , the spatial component is  $a(t)^2 [dr^2 + S_k^2(r) d\Omega^2]$ , and the expansion component is  $\tau^2 \sinh^2 \psi d\psi^2$ . The corresponding metric for  $g_{\mu\nu}$  is:

$$\begin{bmatrix} -1 & 0 & 0 & 0 & 0 \\ 0 & a(t)^2 & 0 & 0 & 0 \\ 0 & 0 & a(t)^2 S_k(r)^2 & 0 & 0 \\ 0 & 0 & 0 & a(t)^2 S_k(r)^2 \sin^2 \theta & 0 \\ 0 & 0 & 0 & 0 & \tau^2 \sinh^2 \psi \end{bmatrix} \quad (21)$$

## 5.2 Christoffel symbols and Ricci curvature

The extra dimension introduces an extra component to Eqs. 14 and 16, with  $dU^\psi/ds$  the time rate of change of the curvature of expansion. The new non-zero Christoffel symbols from Eq. 20 are then given by:

$$\Gamma_{\psi\psi}^t = \tau \dot{\tau} \sinh^2 \psi; \quad \Gamma_{t\psi}^\psi = \Gamma_{\psi t}^\psi = \dot{\tau}/\tau; \quad \Gamma_{\psi\psi}^\psi = 1/\tanh \psi. \quad (22)$$

The non-zero components of the Ricci tensor are now:

$$R_{00} = -3 \frac{\ddot{a}}{a} \quad (23)$$

$$R_{ij} = \left[ \frac{\ddot{a}}{a} + 2 \left( \frac{\dot{a}}{a} \right)^2 + 2 \frac{K}{a^2} + \frac{\dot{a}}{a} \frac{\dot{\tau}}{\tau} \right] g_{ij} \quad (24)$$

$$R_{\psi\psi} = 3 \left( \frac{\dot{a}}{a} \right) \tau \dot{\tau} \sinh^2 \psi \quad (25)$$

and the Ricci curvature is:

$$R = 6 \left[ \frac{\ddot{a}}{a} + \left( \frac{\dot{a}}{a} \right)^2 + \frac{K}{a^2} + \frac{\dot{a}}{a} \frac{\dot{\tau}}{\tau} \right]. \quad (26)$$

A consequence of these new non-zero Christoffel symbols (Eq. 22) is discussed in Section 8.

### 5.3 The Einstein equation and mass-density tensor

$R_{\mu\nu}$  and  $R$  are functions of  $g_{\mu\nu}$  and its first two derivatives. These may now be plugged into the general Einstein equation:

$$R_{\mu\nu} - \frac{1}{2}Rg_{\mu\nu} = \frac{8\pi G}{c^4}T_{\mu\nu} - \frac{\Lambda}{c^2}g_{\mu\nu}, \quad (27)$$

where  $T_{\mu\nu}$  and  $\Lambda$  are the stress-energy tensor and the cosmological expansion parameter respectively, and we assume symmetry with all off-diagonal components = 0.

For an ideal fluid with mass/unit volume  $\rho$  and pressure  $P$ , the stress-energy tensor in the rest frame of the fluid is  $T^\mu{}_\nu = (\rho + P)U^\mu U_\nu + P\delta^\mu{}_\nu$ , or:

$$T_{\mu\nu} = (\rho + P)U_\mu U_\nu + Pg_{\mu\nu}, \quad (28)$$

from which, setting  $c = 1$ , and using  $da/d\tau = a/\tau$  (Fig. 4) and  $\tau^2 = -t^2$ , we may solve Eq. 27 in terms of  $\dot{a}/a$  and  $\ddot{a}/a$ .

$$\left(\frac{\dot{a}}{a}\right)^2 + \frac{K}{a^2} - \frac{1}{t^2} = \frac{8}{3}\pi G\rho + \frac{\Lambda}{3} \quad (29)$$

$$\left(\frac{\dot{a}}{a}\right)^2 + 2\left(\frac{\ddot{a}}{a}\right) + \frac{K}{a^2} - \frac{2}{t^2} = -8\pi GP + \Lambda. \quad (30)$$

or eliminating  $\dot{a}/a$  from Eqs. 29 and 30,

$$H(t)^2 = \frac{8}{3}\pi G\rho - \frac{K}{a^2} + \frac{1}{t^2} + \frac{\Lambda}{3} \quad (31)$$

$$\frac{\ddot{a}}{a} = -\frac{4\pi G}{3}(\rho + 3P) + \frac{1}{2t^2} + \frac{\Lambda}{3}. \quad (32)$$

Defining  $\rho_c \equiv 3H_0^2/8\pi G$  as the critical density of the Universe, and setting Eq. 31 to the present epoch with  $H(t) = H_0$ ,  $a_0 = 1$ , and  $t = T_0$ ,

$$\rho_c = \rho_0 - \frac{3K_0}{8\pi G} + \frac{3}{8\pi GT_0^2} + \frac{\Lambda_0}{8\pi G}, \quad (33)$$

$$\text{and defining: } \Omega_m \equiv \frac{8\pi G\rho_0}{3H_0^2} \quad \Omega_K \equiv -\frac{K}{H_0^2} \\ \Omega_C \equiv \frac{1}{H_0^2 T_0^2} \quad \Omega_\Lambda \equiv \frac{\Lambda}{3H_0^2},$$

Eq. 33 may now be rewritten as  $1 = \Omega_m + \Omega_K + \Omega_C + \Omega_\Lambda$ . Using  $a/a_0 = 1/(1+z)$ ,  $\dot{a}/a = -\dot{z}/(1+z)$ ,  $\rho = \rho_0(a_0/a)^3$ , and the defined density parameters, we may write (Peebles 1993):

$$d_C = \int_{t_0}^{t_e} \frac{dt}{a(t)} = \int_0^z \left(\frac{a}{\dot{a}}\right) dz = \int_0^z \frac{dz}{H_0 E(z)} \quad (34)$$

where  $d_C$  is the comoving distance,  $\dot{a}/a = H_0 E(z)$ , and

$$E(z) = [\Omega_m(1+z)^3 + \Omega_K(1+z)^2 + \Omega_C(1+z)^2 + \Omega_\Lambda]^{1/2}. \quad (35)$$

### 5.4 Solutions

Letting  $\Omega_\Lambda = \Omega_P = 0$ , and assuming a flat Euclidean Universe with  $\Omega_K = 0$ , we may state  $\Omega_C = 1 - \Omega_m$ . This has an analytical solution in  $z$  (Eq. 36),

$$d_C = \frac{c}{H_0} \frac{1}{\sqrt{1 - \Omega_m}} \times \log \left( \frac{(1+z) \left( (1 - 0.5\Omega_m) + \sqrt{1 - \Omega_m} \right)}{1 + 0.5\Omega_m(z-1) + \sqrt{(1 - \Omega_m)(1 + \Omega_m z)}} \right)$$

(36)

which reduces to  $d_C = (c/H_0)\ln(1+z)$  in the Milne limit  $\Omega_m \rightarrow 0$ . This new derivation for  $d_C$  is compared with luminosity distance measures (Section 6) and the recently extended angular diameter distance measures (Section 7). In both cases the modified GR model gives a better fit to the data than the standard  $\Lambda$ CDM model, and is comparable to the best  $w$ -CDM models.

## 6 LUMINOSITY DISTANCE

Correlation between the distance moduli derived from the standard  $\Lambda$ CDM and modified GR model was assessed using the extensive type Ia supernovae (SNe Ia) observations presented by Betoule et al. (2014). This included SN Ia data for 740 sources (Table F.3. Betoule et al. 2014) covering the redshift range  $0.01 \leq z \leq 1.3$ , with data from the Supernova Legacy Survey (SNLS) (Astier et al. 2006); the SDSS SNe survey (Sako et al. 2014); the compilation comprising SNe from SNLS, HST and several nearby experiments (Conley et al. 2011); photometry of 14 very high redshift ( $0.7 < z < 1.3$ ) SNe Ia from space-based observations with the HST (Riess et al. 2007); and low- $z$  ( $z < 0.08$ ) SNe from the photometric data acquired by the Harvard-Smithsonian Center for Astrophysics (CfA3) (Hicken et al. 2009). The corrected apparent brightness parameter  $m_B^*$  of each SN Ia was plotted against its CMB-corrected redshift ( $z_{CMB}$ ) to create the Hubble diagram of Fig. 5. Normalization depends on the assumed absolute magnitude of the SNe and  $H_0$ ; varying either is equivalent to sliding the curves vertically.

Betoule et al. (2014) fitted a  $\Lambda$ CDM cosmology to the SNe measurements by assuming an unperturbed FLRW geometry (Sandage 1988), using a fixed fiducial value of  $H_0 = 70 \text{ km s}^{-1} \text{ Mpc}^{-1}$  ( $M_B = -19.12 \pm 0.05$ ) to obtain a best fit value for  $\Omega_m$  of  $0.295 \pm 0.034$ , with  $\Omega_\Lambda = 0.705$  (blue dashed line). The modified GR model curve (red solid line) was fitted by weighted RMS-minimization to the full data set assuming  $\Omega_m = 0.04$  as the best current assessment of the mean total observed baryonic density of the Universe, and is comparable to that for the  $\Lambda$ CDM model (0.016 and 0.017 respectively). Their  $\Lambda$ CDM model is 0.15 mag fainter than the modified GR model at  $z_{cmb} = 1.0$ , and the two curves differ by  ${}^{+0.11}_{-0.15} m_B^*$  mag over the range  $0.01 < z < 1.3$ .

Betoule et al. (2014) made a substantial effort to correct the distance modulus for each individual SN, using a parameter ( $X_1$ ) for time stretching of the light-curve, and a color-correction parameter ( $C$ ) for the supernova color at maximum brightness (Tripp 1998). Using a corrected distance modulus  $\mu_B = m_B^* - (M_B^* - \alpha X_1 + \beta C)$ , the resultant plots had less scatter than the raw  $m_B^*$  data and became progressively fainter than the  $\Lambda$ CDM curve with increasing  $z_{cmb}$  (Fig. 6). To correct for this, they considered three alternatives to the basic  $\Lambda$ CDM model: (a) a non-zero spatial curvature,  $\Omega_k$ ; (b) a  $w$ -CDM model with an arbitrary constant equation of state for the dark energy with the parameter  $w$  equivalent to the jerk parameter of Riess et al. (2004); (c) a time-dependent equation of state with a third-order term equivalent to the snap parameter,  $w'$  (Riess et al. 2004). They concluded that the best overall fit was to a flat universe with typical  $\Omega_k \approx 0.002 \pm 0.003$ , and a  $w$ -CDM model,

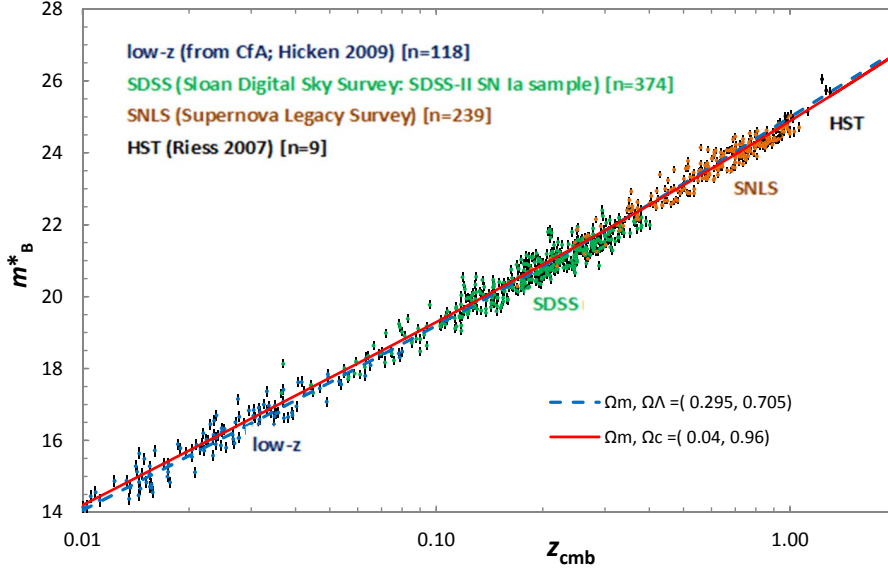


**Figure 5.** Hubble diagram of the combined sample of 920 SNeIa with the observed peak magnitudes in rest frame  $B$ -band ( $m_B^*$ ). Overlain are the best-fit  $\Lambda$ CDM cosmology with  $H_0 = 70 \text{ km s}^{-1} \text{ Mpc}^{-1}$  and  $\Omega_m = 0.295$ ,  $\Omega_\Lambda = 0.705$  (dashed blue line), and the weighted RMS-minimization fit for the modified GR model (red line). Redshifts are corrected to CMB background. (Data points from Betoule et al. 2014)

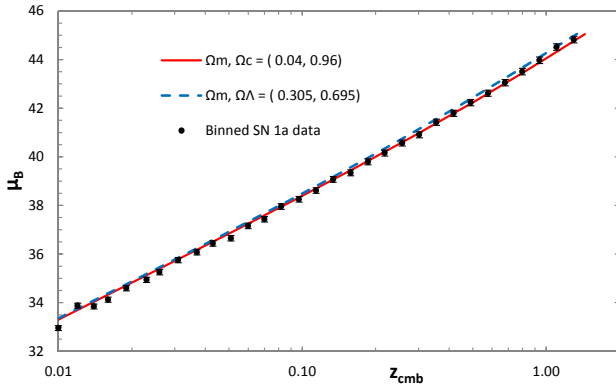


**Figure 6.** Hubble diagram of 920 SNeIa binned logarithmically in  $z_{cmb}$ , with corrected distance moduli  $\mu_B$ . Overlain are the best-fit  $w$ -CDM cosmology with  $\Omega_m = 0.305$ ,  $\Omega_\Lambda = 0.695$  (dashed blue line; RMS error  $\pm 0.151 \mu_B$  mag), and the unweighted least-squares fit for the modified GR model (red line; RMS error  $\pm 0.136 \mu_B$  mag) (data from Table F.1. Betoule et al. 2014).

with  $w = -1.018 \pm 0.057$  (stat+sys), and with these corrections, their  $w$ -CDM curve overlays the binned plots at the faint end (Fig. 6). The modified GR model was normalized to the standard model at  $z = 0.01$ . The overall unweighted RMS errors remain comparable for the  $w$ -CDM and modified GR models, being 0.151 and 0.136  $\mu_B$  mag. respectively, differing by  $^{+0.00}_{-0.24} \mu_B$  mag. over the range  $z_{cmb} = 0.01 - 1.3$ .

## 7 ANGULAR DIAMETER DISTANCE

Angular diameter distance  $d_A$  is defined for an object of known proper size  $D$ , that subtends an angle  $\phi$  to the observer such that

$$d_A = D/\phi. \quad (37)$$

If a suitable measuring rod can be found which is independent of galactic evolution, then the points of  $D$  are fixed in space and lie on the surface of the space-like sphere defined by the proper radius  $\mathfrak{R}_e$  of Fig. 1, where we may identify  $\mathfrak{R}_e$  with the angular size distance. This may be used with the standard expression for  $d_A$  (Hogg 2000; Bonamente et al. 2006), in terms of  $d_C$  from equation (34):

$$d_A = \frac{d_C}{(1+z)}. \quad (38)$$

Experimental verification of curves of this type is notoriously difficult because of the unknown evolution of galaxies, clusters and quasars (Bonamente et al. 2006; Ruhl et al. 2004; Bleem et al. 2015), but recent work using the phenomenon of baryonic acoustic oscillation has enabled measurements of  $d_A$  with considerable accuracy.

### 7.1 Baryon acoustic oscillations

The baryon acoustic oscillation (BAO) signal is one of the key modern methods for measuring the expansion history. The BAO arose because the coupling of baryons and photons in the early Universe allowed acoustic oscillations to develop that led to anisotropies of the cosmic microwave background (CMB) radiation and a rich structure in the distribution of matter (Glazebrook & Blake 2005; Anderson et al. 2012). The acoustic scale length ( $r_S$ ) can be computed as the comoving distance that the sound waves could travel

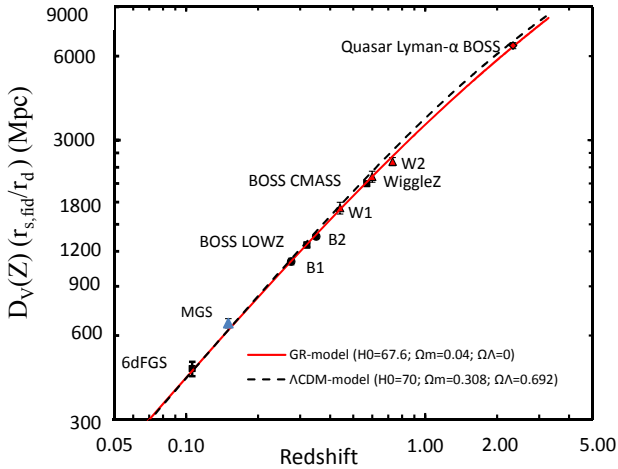


**Figure 7.** A plot of the distance-redshift relation from various BAO measurements from several spectroscopic data sets, and quasar Lyman- $\alpha$  BOSS, plotting  $D_V(z)(r_{s, fid}/r_d)$  (Beutler et al. 2011; Ross et al. 2015; Percival et al. 2010; Anderson et al. 2014; Cuesta et al. 2016; Padmanabhan et al. 2012; Xu et al. 2013; Kazin et al. 2014; Font-Ribera et al. 2014). Overlain are the best-fitting flat  $\Lambda$ CDM  $1-\sigma$  prediction from WMAP under the assumption of a flat universe with a cosmological constant ( $\Omega_m = 0.308$ ;  $\Omega_\Lambda = 0.692$ ) (Komatsu et al. 2011; Anderson et al. 2012) (dashed line) and the modified GR model fitted by weighted RMS-minimization to  $H_0 = 67.6 \pm 0.25$  with  $\Omega_m = 0.04$ ,  $\Omega_C = 0.96$  (solid line)

from the Big Bang until recombination. The imprint left by these sound waves provides a feature of known size in the late-time clustering of matter and galaxies, and by measuring this acoustic scale at a variety of redshifts, one can infer  $d_A(z)$  and  $H(z)$ .

Determination of  $r_s$  comes from the matter-to-radiation ratio and the baryon-to-photon ratio, both of which are well measured by the relative heights of the acoustic peaks in the CMB anisotropy power spectrum (Eisenstein et al. 1998; Weinberg et al. 2013). Both cosmological perturbation theory and numerical simulations suggest that this feature is stable to better than 1% accuracy, making it an excellent standard ruler. The propagation distance of the acoustic waves becomes a characteristic comoving scale fixed by the recombination time of the Universe after approximately 379,000 years, at a redshift of  $z = 1089$  (Peebles & Yu 1970; Sunyaev & Zeldovich 1970; Doroshkevich et al. 1978). Eisenstein et al provide a discussion of the acoustic signal in configuration space (Eisenstein et al. 2007), and reviews of BAO as a probe of dark energy (Eisenstein & Bennett 2008). The acoustic scale is expressed in absolute units (Mpc) rather than  $h^{-1}$  Mpc, and is imprinted on very large scales ( $\sim 150$  Mpc) thereby being relatively insensitive to small scale astrophysical processes, making BAO experiments less sensitive to this type of systematic error (Weinberg et al. 2013).

Figure 7 combines the BAO results from a number of sources using spectroscopic data sets, and the quasar Lyman- $\alpha$  results from the SDSS-III Baryon Oscillation Spectroscopic Survey (BOSS). The volume  $D_V(z)$  corresponds

**Table 1.** Detailed parameters from the BAO surveys

Survey	$z$	$D_V(r_d/r_{d, fid})$ (Mpc)
6dFGS <sup>1</sup>	0.106	456 $\pm$ 27
MGS <sup>2</sup>	0.15	664 $\pm$ 25
BOSS (B1) <sup>3</sup>	0.275	1104 $\pm$ 30
BOSS LowZ <sup>4</sup>	0.32	1264 $\pm$ 25
BOSS (B2) <sup>5</sup>	0.35	1356 $\pm$ 25
WigglerZ (W1) <sup>6</sup>	0.44	1716 $\pm$ 83
CMASS <sup>4</sup>	0.57	2056 $\pm$ 20
WigglerZ (W2) <sup>6</sup>	0.6	2221 $\pm$ 101
WigglerZ <sup>6</sup>	0.73	2516 $\pm$ 86
Lyman- $\alpha$ forest <sup>7</sup>	2.36	6474 $\pm$ 163

<sup>1</sup>Beutler et al. (2011); <sup>2</sup>Ross et al. (2015); <sup>3</sup>Percival et al. (2010); <sup>4</sup>Anderson et al. (2014); Cuesta et al. (2016); <sup>5</sup>Padmanabhan et al. (2012); Xu et al. (2013); <sup>6</sup>Kazin et al. (2014); <sup>7</sup>Font-Ribera et al. (2014)

to the peak position for an isotropic distribution of galaxy pairs and the 2-point isotropic clustering strength  $\xi(z)$  of the observations, computed using Eq. (39) to convert the line-of-sight distance into an equivalent transverse length scale, where  $d_A$  is the angular diameter distance and  $H(z)$  is the Hubble parameter in the appropriate model. As the BAO method actually measures  $D_V/r_d$ , this quantity was multiplied by the fiducial scale length  $r_{s, fid}$  to restore a distance (Anderson et al. 2012; Eisenstein et al. 2005).

$$D_V \equiv [d_A^2 \times \frac{cz}{H(z)} (1+z)^2]^{1/3} \quad (39)$$

Included are the acoustic peak detection from the 6dF Galaxy Survey at  $z = 0.106$  (Beutler et al. 2011); the MGS survey at  $z = 0.15$  (Ross et al. 2015); a combination of Sloan Digital Sky Survey (SDSS)-II DR7 LRG and main sample galaxies combined with the 2dF data (B1) at  $z = 0.275$  (Percival et al. 2010); the BOSS CMASS measurements at  $z = 0.32$  and  $z = 0.57$  (Anderson et al. 2014; Cuesta et al. 2016); the SDSS-II LRG (B2) measurement at  $z = 0.35$  using reconstruction to sharpen the precision of the BAO measurement (Padmanabhan et al. 2012; Xu et al. 2013); and the WigglerZ measurement of three partially covariant data sets at  $z = 0.44$ , 0.6, and 0.73 (Kazin et al. 2014). The published values for  $D_V(z)$  are presented in Table 1. Font-Ribera et al (Font-Ribera et al. 2014) measured the large-scale cross-correlation of quasars with the Lyman- $\alpha$  forest absorption, using over 164,000 quasars from DR11 of the SDSS-III BOSS. Their result was an absolute measure of  $d_A = 1590 \pm 60$  Mpc at  $z = 2.36$ , that translates to  $D_V = 6474 \pm 163 (r_d/r_{s, fid})$  Mpc, with  $r_d = 147.49$  Mpc.

Also plotted in Fig. 7 are curves for the two models. The dashed line is the best-fitting  $\Lambda$ CDM prediction from WMAP under the assumption of a flat universe with a cosmological constant using data provided by the Planck Collaboration ( $\Omega_m = 0.308 \pm 0.012$ ;  $\Omega_\Lambda = 0.692 \pm 0.012$ ;  $\Omega_K = 0$ ) (Table 4, Planck Collaboration et al. 2016a). The solid curve is the modified GR model with  $\Omega_m = 0.04$ ,  $\Omega_C = 0.96$ . As in Section 6, changing  $H_0$  slides the curves up or down the vertical axis, but does not alter the shapes of the curves which were fitted by weighted RMS minimization against the combined BAO samples of Table 1 to give  $H_0 = 70.0 \pm 0.25$  and

$H_0 = 67.6 \pm 0.25$  for the  $\Lambda$ CDM and modified GR models respectively. The uncertainties in the two lines come largely from uncertainties in  $\Omega_m h^2$ . The weighted RMS errors were  $\pm 0.085$  Mpc for the  $\Lambda$ CDM model and  $\pm 0.034$  Mpc for the modified GR model, although as with the luminosity distance measures, the standard model can be improved with non-linear parameters added to  $\Omega_\Lambda$  in a  $w'$ -CDM model.

## 8 DISCUSSION

A central tenet of GR is that it is always valid to choose a coordinate system that is locally Minkowskian. [Bunn & Hogg \(2009\)](#) have suggested that the stretching-of-space interpretation obscures this central idea, and showed that the observed cosmological redshift can be interpreted as either a gravitational redshift, or a kinematic redshift by the integration of infinitesimal Doppler shifts. Performing such a transport along the null geodesic of photons arriving from a receding galaxy, they considered that the frequency shift is purely kinematic, corresponding to a family of comoving observers, and hence was more natural. This idea was developed further by [Chodorowski \(2011\)](#) who suggested that the frequency shift coincides with decomposition into a Doppler (kinematic) component and a gravitational one, and by [Kaiser \(2014\)](#) who suggested that even where gravitational redshift dominates, redshift can always be formally expressed using the Doppler formula. The modified GR model incorporates both kinematic and gravitational components as  $\Omega_C$  and  $\Omega_m$  respectively, with parallel transport along the photon path, and rotation across curved diverging time lines.

By considering GR as a geometrical manifold with an imaginary time-axis, adjacent photon paths trace out a thin ribbon that everywhere subtends an angle of  $45^\circ$  to the expanding time axes, this being the locally Minkowskian metric. In a static Universe with no relative velocity between emitter and receiver, this is a plane Euclidean quadrilateral with parallel photon paths and time-lines, and it retains this form when wrapped round a cylinder. In the SR model of Figs. 1 and 2 this ribbon becomes curved and stretched by both the relative velocity and by any intrinsic curvature of space to produce the observed redshift. This curvature, however, can still be wrapped round a uniform cone. In the Milne model, redshift is accounted for solely by the relative velocities. In contrast, the presence of mass-energy represented by  $\rho_0$  and  $P$  generates an additional curvature and twist in the ribbon (Figs. 3 and 4) that require Einstein's equations and are generally solved using the standard FLRW metric.

Assuming spatial curvature to be zero, the observed matter in the Universe is insufficient to account for the measured redshifts and requires the inclusion of an additional dark-matter component, while to conform to the more detailed SNe 1a measurements of [Perlmutter et al. \(1999\)](#) an additional dark-energy term ( $\Lambda$ ) is included, mathematically equivalent to a negative, gravitationally repulsive, mass. Deeper and more detailed SNe 1a measurements ([Riess et al. 2004](#); [Betoule et al. 2014](#)) have required second and third order refinement to  $\Lambda$ , with jerk and snap parameters.

While the nature of dark matter and dark energy remain elusive, several alternative theories to standard GR have emerged such as [Maeder \(2017\)](#), who explores scale invari-

ance as an alternative to dark energy. However, recently published work following the observation of gravitational waves from the binary neutron star GW170817 ([The LIGO Scientific Collaboration et al. 2017](#)) have determined  $c_g$  with sufficient accuracy to suggest that  $c_g = c \pm 10^{-15}$ . This has eliminated several gravitational theories that predict an anomalous  $c_g$  propagation speed such as some MOND-like gravities and TeVeS, Hernández forms, Einstein-Aether, Generalized Proca, Hořava gravity, and some alternative scenarios proposed to account for the unobserved dark energy fraction of Einstein's equation ([María Ezquiaga & Zumalacárregui 2017](#); [Sakstein & Jain 2017](#); [Lombriser & Lima 2017](#)).

The introduction of a curvature term into Einstein's equation follows directly from geometrical considerations of the expansion of space, and is a logical extension of GR. The use of  $\Omega_C$  as a curvature term allows a smooth transition from GR to SR as density decreases, without requiring a discontinuity in the curvature parameter,  $\Omega_K$ . The introduction of  $\Omega_C$  generates a magnitude-redshift curve that well matches current SNe 1a observations out to  $z = 1.3$ , assuming only that  $\rho_m$  represents observable baryonic mass. Comparing the modified GR model for angular diameter distances to BAO measurements also gives an excellent fit at low- $z$ , continuing to  $z = 2.36$ , without requiring additional parameters. Using weighted RMS-minimization fitting to the combined BAO samples of Table 1 gave  $H_0 = 67.6 \pm 0.25$ .

Non-zero Christoffel symbols are imposed by any acceleration, whether caused by a gravitational field, by the action of fields other than those associated with gravitational mass, or by curvilinear motion of the body ([Weinberg 1972](#)). The emergence of new non-zero Christoffel symbols (Eq. 22) supports the presence of curvilinear motion imposed on the red-shifted photons by the expansion of space, and is distinct from the curvature of space by the presence of mass. The two curvature terms,  $\Omega_K$  and  $\Omega_C$ , are derived from very different principles, the former being an intrinsic curvature within space itself, while the latter requires an extension to the standard model. Nevertheless, it may be noted that there is a mathematical correspondence between the two that may imply an identity with  $K = -(cT_0)^{-2}$ . If so, this identity may arise at a fundamental level, implying that expanding space is not Euclidean with  $\Omega_K = 0$  but hyperbolically curved by the expansion itself, modified by the presence of its contained mass-energy. While several theoretical predictions propose the existence of DM to address the mass discrepancy problem in the Universe and within galaxies, the extension to GR proposed in this paper can accommodate a scenario in which the observations of SNe 1a and BAO may not require any additional parameters from DM or accelerating dark energy.

## REFERENCES

- Anderson L., Aubourg E., Bailey S., Bizyaev D., Blanton M., Bolton A. S., et al 2012, [MNRAS](#), **427**, 3435  
Anderson L., Aubourg É., Bailey S., Beutler F., Bhardwaj V., Blanton M., et al 2014, [MNRAS](#), **441**, 24  
Astier P., Guy J., Regnault N., Pain R., Aubourg E., Balam D., et al 2006, [A&A](#), **447**, 31  
Betoule M., Kessler R., Guy J., Mosher J., Hardin D., Biswas R., et al 2014, [A&A](#), **568**, A22

- Beutler F., Blake C., Colless M., Jones D. H., Staveley-Smith L., Campbell L., et al 2011, *MNRAS*, **416**, 3017
- Bleem L. E., Stalder B., de Haan T., Aird K. A., Allen S. W., Applegate D. E., et al 2015, *ApJS*, **216**, 27
- Bonamente M., Joy M. K., LaRoque S. J., Carlstrom J. E., Reese E. D., Dawson K. S., 2006, *ApJ*, **647**, 25
- Bromley B. C., Kenyon S. J., Brown W. R., Geller M. J., 2009, *ApJ*, **706**, 925
- Bunn E. F., Hogg D. W., 2009, *AmJPhys*, **77**, 688
- Carroll S. M., 2003, *An Introduction to General Relativity Space-time and Geometry*. Addison-Wesley, San Francisco
- Chodorowski M. J., 2011, *MNRAS*, **413**, 585
- Conley A., Guy J., Sullivan M., Regnault N., Astier P., Balland C., et al 2011, *ApJS*, **192**, 1
- Cottam J., Paerels F., Mendez M., 2002, in Branduardi-Raymont G., ed., *High Resolution X-ray Spectroscopy with XMM-Newton and Chandra*.
- Crowell B., 2012, *General Relativity*. Fullerton, www.lightandmatter.com, California
- Cuesta A. J., Vargas-Magaña M., Beutler F., Bolton A. S., Brownstein J. R., Eisenstein D. J., et al 2016, *MNRAS*, **457**, 1770
- Doroshkevich A. G., Zel'dovich Y. B., Syunyaev R. A., 1978, *Soviet Ast.*, **22**, 523
- Eisenstein D. J., Bennett C. L., 2008, *Physics Today*, **61**, 44
- Eisenstein D. J., Hu W., Tegmark M., 1998, *ApJ*, **504**, L57
- Eisenstein D. J., Zehavi I., Hogg D. W., Scocimarro R., Blanton M. R., Nichol R. C., et al 2005, *ApJ*, **633**, 560
- Eisenstein D. J., Seo H.-J., White M., 2007, *ApJ*, **664**, 660
- Figueras P., Kunesch M., Tunyasuvunakool S., 2016, *Phys. Rev. Lett.*, **116**, 071102
- Font-Ribera A., Kirkby D., Busca N., Miralda-Escudé J., Ross N. P., Slosar A., et al 2014, *J. Cosmology Astropart. Phys.*, **5**, 027
- Glazebrook K., Blake C., 2005, *ApJ*, **631**, 1
- Hicken M., Challis P., Jha S., Kirshner R. P., Matheson T., Modjaz M., et al 2009, *ApJ*, **700**, 331
- Hogg D. W., 2000, arXiv:astro-ph/0001419,
- Kaiser N., 2014, *MNRAS*, **438**, 2456
- Kazin E. A., Koda J., Blake C., Padmanabhan N., Brough S., Colless M., et al 2014, *MNRAS*, **441**, 3524
- Komatsu E., Smith K. M., Dunkley J., Bennett C. L., Gold B., Hinshaw G., et al 2011, *ApJS*, **192**, 18
- Komissarov S. S., 2009, *General Relativity*. <https://www1.maths.leeds.ac.uk/~serguei/teaching/sr.pdf>
- Lombriser L., Lima N. A., 2017, *Physics Letters B*, **765**, 382
- Maeder A., 2017, *ApJ*, **834**, 194
- María Ezquiaga J., Zumalacárregui M., 2017, arXiv:1710.05901,
- Marr J. H., 2016, *Int. J. Mod. Phys. C*, **27**, 1650055
- Milne E. A., 1935, *Relativity, Gravitation and World Structure*. OUP, Oxford, UK
- Milnor J., 2003, *NOTICES OF THE AMS*, **50**, 1226
- Misner C. W., Thorne K. S., A. W. J., 1970, *Gravitation*. W. H. Freeman and Company, San Francisco
- Müller A., Camenzind M., 2004, *A&A*, **413**, 861
- Padmanabhan N., Xu X., Eisenstein D. J., Scalzo R., Cuesta A. J., Mehta K. T., Kazin E., 2012, *MNRAS*, **427**, 2132
- Peebles P. J. E., 1993, *Principles of Physical Cosmology*. Princeton University Press, Princeton NJ
- Peebles P. J. E., Yu J. T., 1970, *ApJ*, **162**, 815
- Percival W. J., Reid B. A., Eisenstein D. J., Bahcall N. A., Budavari T., Frieman J. A., et al 2010, *MNRAS*, **401**, 2148
- Perelman G., 2008, arXiv:math/0303109v1
- Perlmutter S., Aldering G., Goldhaber G., Knop R. A., Nugent P., Castro P. G., et al 1999, *ApJ*, **517**, 565
- Planck Collaboration Ade P. A. R., Aghanim N., Arnaud M., Ashdown M., Aumont J., Baccigalupi C., et al. 2016a, *A&A*, **594**, A13
- Planck Collaboration Ade P. A. R., Aghanim N., Arnaud M., Ashdown M., Aumont J., Baccigalupi C., et al. 2016b, *A&A*, **594**, A24
- Reynolds M. T., Reis R. C., Miller J. M., Cackett E. M., Degenaar N., 2014, *MNRAS*, **441**, 3656
- Riess A. G., Strolger L.-G., Tonry J., Casertano S., Ferguson H. C., Mobasher B., et al 2004, *ApJ*, **607**, 665
- Riess A. G., Strolger L.-G., Casertano S., Ferguson H. C., Mobasher B., Gold B., et al 2007, *ApJ*, **659**, 98
- Ross A. J., Samushia L., Howlett C., Percival W. J., Burden A., Manera M., 2015, *MNRAS*, **449**, 835
- Ruhl J., Ade P. A. R., Carlstrom J. E., Hsiao-Mei Cho H., et al. 2004, *The South Pole Telescope*, doi:10.1117/12.552473, <http://dx.doi.org/10.1117/12.552473>
- Sako M., Bassett B., Becker A. C., Brown P. J., Campbell H., Cane R., et al 2014, arXiv:astro-ph.CO/1401.3317,
- Sakstein J., Jain B., 2017, *Physical Review Letters*, **119**, 251303
- Sandage A., 1988, *ARA&A*, **26**, 561
- Sunyaev R. A., Zeldovich Y. B., 1970, *Ap&SS*, **7**, 3
- The LIGO Scientific Collaboration et al., 2017, *Ap. J. Letters*, **848**, L12
- Tripp R., 1998, *A&A*, **331**, 815
- Weinberg S., 1972, *Gravitation and Cosmology: Principles and Applications of the General Theory of Relativity*. Wiley, New York
- Weinberg D. H., Mortonson M. J., Eisenstein D. J., Hirata C., Riess A. G., Rozo E., 2013, *Phys. Rep.*, **530**, 87
- Wong K. C., Suyu S. H., Matsushita S., 2015, *ApJ*, **811**, 115
- Xu X., Cuesta A. J., Padmanabhan N., Eisenstein D. J., McBride C. K., 2013, *MNRAS*, **431**, 2834

This paper has been typeset from a  $\text{\TeX}/\text{\LaTeX}$  file prepared by the author.